



Absorption and scattering limits of silicon nitride integrated photonics in the visible spectrum

MATEUS CORATO-ZANARELLA,^{1,4} XINGCHEN JI,^{1,2} ASEEMA MOHANTY,^{1,3} AND MICHAL LIPSON^{1,5}

¹Department of Electrical Engineering, Columbia University, New York, New York 10027, USA

²John Hopcroft Center for Computer Science, Shanghai Jiao Tong University, Shanghai 200240, China

³Department of Electrical and Computer Engineering, Tufts University, Medford, MA 02155, USA

⁴mcz2109@columbia.edu

⁵ml3745@columbia.edu

Abstract: Visible-light photonic integrated circuits (PICs) promise scalability for technologies such as quantum information, biosensing, and scanning displays, yet extending large-scale silicon photonics to shorter wavelengths has been challenging due to the higher losses. Silicon nitride (SiN) has stood out as the leading platform for visible photonics, but the propagation losses strongly depend on the film's deposition and fabrication processes. Current loss measurement techniques cannot accurately distinguish between absorption and surface scattering, making it difficult to identify the dominant loss source and reach the platform's fundamental limit. Here we demonstrate an ultra-low loss, high-confinement SiN platform that approaches the limits of absorption and scattering across the visible spectrum. Leveraging the sensitivity of microresonators to loss, we probe and discriminate each loss contribution with unparalleled sensitivity, and derive their fundamental limits and scaling laws as a function of wavelength, film properties and waveguide parameters. Through the design of the waveguide cross-section, we show how to approach the absorption limit of the platform, and demonstrate the lowest propagation losses in high-confinement SiN to date across the visible spectrum. We envision that our techniques for loss characterization and minimization will contribute to the development of large-scale, dense PICs that redefine the loss limits of integrated platforms across the electromagnetic spectrum.

© 2024 Optica Publishing Group under the terms of the [Optica Open Access Publishing Agreement](#)

1. Introduction

Visible-light photonic integrated circuits (PICs) promise scalability for technologies such as quantum information [1–3], biosensing [4–6], and scanning displays [7–9]. However, extending large-scale silicon photonics to the visible spectrum is challenging due to the higher propagation losses at short wavelengths. The stronger absorption and roughness-induced scattering place stringent constraints on the materials and fabrication processes for realizing high-confinement waveguides. In fact, most materials with large transparency window are not currently compatible with photonic foundries and are difficult to etch, such as lithium niobate (LiNbO_3) [10], aluminum nitride (AlN) [11–14], aluminum oxide (Al_2O_3) [15,16] and titanium dioxide (TiO_2) [17,18]. While low-confinement platforms achieve ultra-low loss by delocalizing the optical mode into the silicon dioxide (SiO_2) cladding [19–22], they are unsuitable for dense and scalable PICs as they require mm-to-cm-scale bending radii and thick claddings [23,24]. Moreover, due to the minimal modal overlap with the ultra-thin silicon nitride core, they are incompatible with the strong optical confinement required by foundational devices and applications, such as efficient modulators [25,26] and phase shifters [27], nonlinear optics [28], and dispersion engineering [23,24].

High-confinement silicon nitride (SiN) is the leading material platform for visible integrated photonics due to its wide transparency window, smooth etching, strong confinement, depositability, and foundry-compatibility [23,29]. It has enabled high-performance fundamental components such as integrated lasers [30], efficient phase shifters [27], couplers [4,5,31], splitters [4,5] and photodetectors [32]. However, the SiN's deposition conditions strongly affect the film's properties and response to fabrication processes [33,34], resulting in highly variable propagation losses [5,16,30,32,35–51]. Such tunability makes it challenging to identify the dominant source of loss using current measurement techniques, hindering our ability to approach the platform's fundamental limit. Figure 1 shows loss measurements for two low-pressure chemical vapor deposition (LPCVD) SiN films with different Si/N ratios. Although ellipsometry (Fig. 1(a)) reveals a larger transparency window for the N-richer film, it fails to detect the extended absorption tail that limits the propagation losses in the visible and near-infrared (near-IR) ranges, as illustrated by the 4-5 times difference in quality factors (Q) for identical microresonators made of the films (Fig. 1(b)). While this difference is due to film absorption, the resonator losses are also affected by surface scattering, which strongly depends on the microfabrication quality and the wavelength of light. It is therefore unclear which contribution dominates and limits the propagation losses of the integrated devices. Current loss measurement techniques, such as ellipsometry [33,52], cutback [5,16], outscattered light [35,50], and photothermal spectroscopy [19,53], cannot extract absorption and scattering independently or with enough sensitivity for arbitrary ultra-low loss thin films (Supplement 1, section 1). Without precisely quantifying the sources of loss, it is impossible to determine the platform's fundamental limit and devise a strategy to approach it.

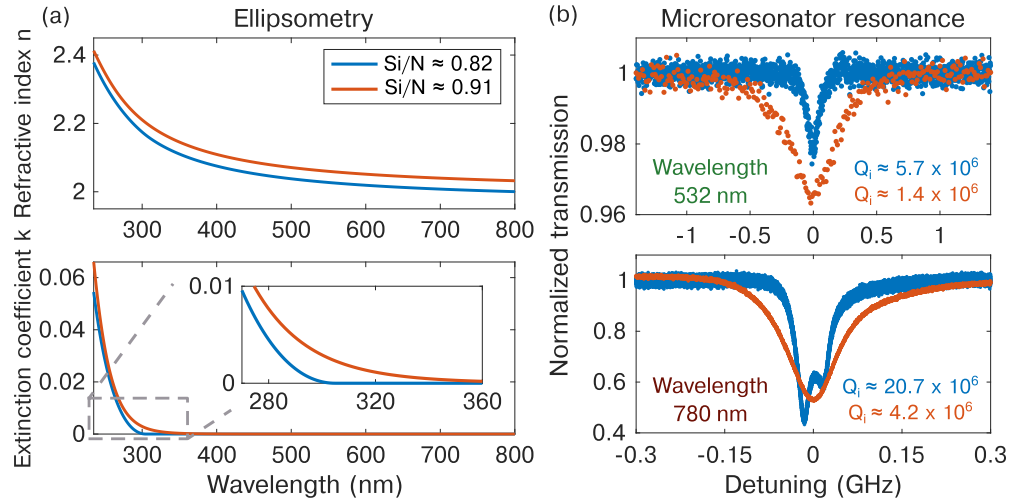


Fig. 1. Characterization of two LPCVD SiN films and microresonators with varying elemental compositions. (a) Refractive index (top) and extinction coefficient (bottom) of the films measured via ellipsometry (Si/N ratios indicated in the legend). The N-richer film is nominally transparent over a larger spectral window (bottom inset). We present details of the optical and compositional measurements in Supplement 1, section 2. (b) Resonances of microring resonators with $4 \mu\text{m}$ width and $300 \mu\text{m}$ radius fabricated with the two SiN films using the same fabrication processes (Methods, section 5.1). The contrasting Q s show that ellipsometry cannot detect the loss difference between the films within the visible (top, 532 nm wavelength) and near-IR (bottom, 780 nm wavelength) regions.

2. Main

Here we demonstrate an ultra-low loss, high-confinement SiN platform that approaches the

limits of absorption and scattering across the visible spectrum. We leverage the ultra-high Q microresonators to probe and discriminate each loss contribution with unparalleled sensitivity, enabling the derivation of their fundamental limits and scaling laws as a function of wavelength, film properties and waveguide parameters. In order to extract the components of the propagation loss, we fabricate and measure the Q of microring resonators with varying widths (400 nm, 500 nm, 750 nm, 1000 nm, 2000 nm, 4000 nm) and radii (30 μm , 55 μm , 115 μm , 300 μm) for the SiN film with Si/N = 0.82 (blue curves in Fig. 1(a)) at wavelengths from deep blue to near-IR (461 nm, 488 nm, 532 nm, 644 nm, and 780 nm) for TE and TM polarizations. The modal overlap with the sidewalls decreases as the width and radius of the microresonator increase, thus reducing the scattering loss and approaching the absorption limit (Fig. 2(a)). Mathematically, we describe the propagation loss coefficient of the mode of a narrow reference waveguide (e.g. Figure 2(a), left panel) as

$$\alpha^{(0)} = \alpha_{abs} + \alpha_{sides} + \alpha_{top} + \alpha_{bottom} \quad (1)$$

where α_{abs} , α_{sides} , α_{top} and α_{bottom} correspond respectively to the absorption, sidewalls scattering, top wall scattering, and bottom wall scattering contributions. For another waveguide with larger width (e.g. Figure 2(a), right panel), the propagation loss of a mode (n) is given by

$$\alpha^{(n)} = \eta_{abs}^{(n)} \alpha_{abs} + \eta_{sides}^{(n)} \alpha_{sides} + \eta_{top}^{(n)} \alpha_{top} + \eta_{bottom}^{(n)} \alpha_{bottom} \quad (2)$$

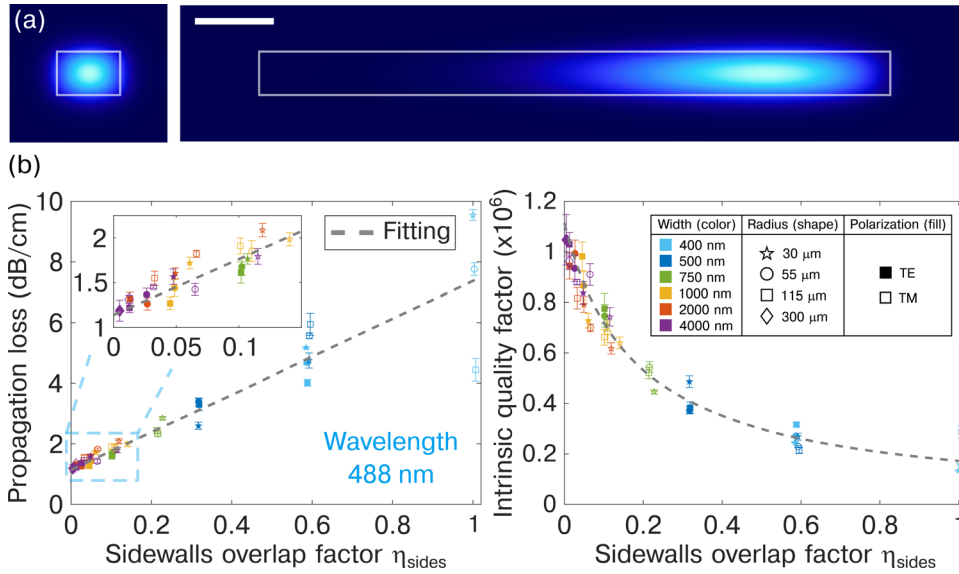


Fig. 2. Effect of the waveguide cross-section on the mode propagation loss at 488 nm wavelength. (a) Field amplitude of the fundamental TE modes of narrow (left, 400 nm width and 30 μm radius) and wide (right, 4000 nm width and 300 μm radius) microresonators, showing that the modal overlap with the sidewalls decreases as the width increases. Scale bar: 500 nm. (b) Measured propagation losses (left) and corresponding intrinsic quality factors (right) as a function of the overlap with the sidewalls referenced to the narrowest waveguide (η_{sides}). The slope relates to the strength of the surface scattering, while the intercept relates to the material absorption. The errorbars correspond to the mean \pm s.d. of tens of consecutive measurements for all the recorded laser detunings of each resonance (e.g., Fig. 3(b)). We present a detailed discussion of the loss model and the datasets for the other wavelengths in [Supplement 1](#), sections 4 and 5.

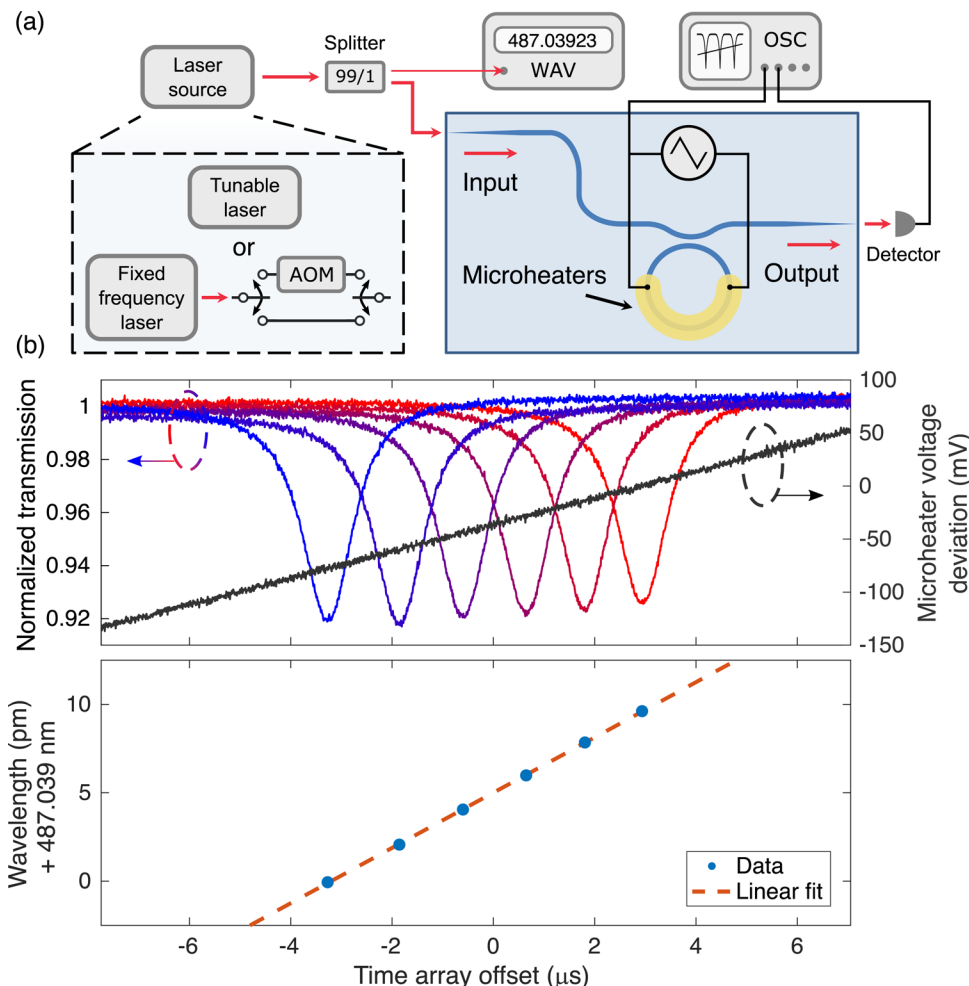


Fig. 3. Microresonator measurement scheme using microheaters and lasers. (a) Schematic of the experimental setup. We couple a laser source with a static wavelength to the PIC, where we modulate the ring's microheater with a triangular voltage of 10 kHz frequency. We simultaneously monitor the wavelength of the laser with a wavemeter, the microheater voltage with an oscilloscope, and the microresonator transmission with a photodetector. The laser source is either a tunable laser or a fixed-frequency laser coupled to an AOM (Methods, section 5.2). (b) Resonance measurement procedure, in which we step-wise tune the laser source while recording the signals in (a). Each laser wavelength (bottom) maps to a different resonance position relative to the voltage trigger (top), providing a calibration to extract the linewidth.

where $\eta_{abs}^{(n)}$, $\eta_{sides}^{(n)}$, $\eta_{top}^{(n)}$, and $\eta_{bottom}^{(n)}$ account for the mode interaction with the waveguide core, sidewalls, top wall, and bottom wall relative to the reference waveguide, respectively (Supplement 1, section 5A). Radiation loss is neglected since the microring radii are large enough to prevent it. Since the top and bottom surfaces are at least an order of magnitude smoother than the sidewalls ($\alpha_{top} + \alpha_{bottom} \ll \alpha_{sides}$, Supplement 1 section 5A) and the modal confinement remains approximately constant ($\eta_{abs}^{(n)} \approx 1$, Supplement 1 section 5A), the propagation loss scales approximately linearly with $\eta_{sides}^{(n)}$ (Fig. 2(b)), with slope and intercept related to α_{sides} and α_{abs} respectively. By calculating $\alpha^{(n)}$ from the measured Qs (Supplement 1, section 3) and fitting them

using (2), we independently extract the absorption (α_{abs}) and scattering (α_{sides}) loss components for each wavelength with high sensitivity ([Supplement 1](#) section 5).

We use a combination of microheater and laser tuning to measure the microring resonances at visible wavelengths (Fig. 3), decoupling the resonance scanning speed from the wavelength tuning and measurement rates. We design the microresonators with a point-coupling scheme and measure resonances with small extinctions (Fig. 5) to eliminate coupling region-induced loss [30,54], thus correctly probing the resonators' intrinsic losses. In order to achieve high transmission sensitivity down to 2% (Fig. 5(b), center panel) over large detuning ranges, we modulate the microheater with high speed (10 kHz rate, Fig. 3(a)) and large amplitude, and calibrate the detuning by step-wise tuning the laser wavelength (Fig. 3(b)). In contrast to slowly scanning a laser (e.g., 100 Hz rate) across a resonance, such as in our near-IR (780 nm) measurements, our hybrid approach overcomes the constraints from the typical sub-kHz laser modulation bandwidth and the milliseconds-long exposure times of wavemeters [30], eliminating low-frequency noise that limits resonance visibility and extinction measurement sensitivity. For a fixed microheater triangular voltage, we record the resonator transmission for detuned input wavelengths (Fig. 3(b)), either by employing a tunable laser (461 nm, 488 nm, 644 nm center wavelengths) or a fixed-frequency laser (532 nm) coupled to an acousto-optic modulator (AOM) (Methods, section 5.2). For each laser wavelength (Fig. 3(b), bottom), the resonance moves to a different position relative to the voltage trigger (Fig. 3(b), top), providing a map between the voltage and the optical frequency detuning. Using this calibration, we extract the linewidth of the resonance. We drive the microheater with a high resolution waveform generator (Methods, section 5.2) to ensure an effectively continuous voltage ramp able to resolve ultra-narrow linewidths without quantization noise. Since the continuous tuning range is provided by the microheaters instead of the laser, our strategy enables using laser sources with slow or limited tuning capabilities, such as fixed-frequency lasers coupled to AOMs or nonlinear frequency-converting systems. As such, our approach can be applied to spectral ranges where tunable lasers are not readily available, for example within the “green gap” [55]. In contrast to other approaches employing microheaters [11], our wavelength calibration method does not require knowledge of geometrical and material properties, making it applicable to any material platform and spectral range.

3. Results

We extract the fundamental absorption (Fig. 4(a)) and surface scattering (Fig. 4(b)) loss limits of the SiN platform across the visible spectrum, and demonstrate that by increasing the waveguide width we can move from a scattering-dominated to an absorption-dominated loss regime by design (Fig. 4(c)). We show that the material absorption of SiN follows a band-fluctuations model [56] (Fig. 4(a)), and that the sidewall scattering per unit of overlap follows a normalized version of the Payne-Lacey (NPL) model [57,58] that can also be well fitted by a power law of the type $\lambda^{-2.3}$ (Fig. 4(b)). Our microring-based characterization strategy not only quantifies the loss limits by discriminating absorption and surface scattering, but also detects absorption with nearly five orders of magnitude higher sensitivity than standard ellipsometric measurements of thin films [59] (orange dashed line in Fig. 4(a)). From the absorption fitting, we extract the optical bandgap of the SiN film (E_g) to be around 4.63 eV with an Urbach slope (β) of 5.07 eV⁻¹ ([Supplement 1](#), section 5B), which is consistent with values reported in the literature [60]. The NPL fitting of the scattering results in a root mean square (RMS) roughness (σ) of 1.5 nm and a correlation length (L_c) of 90 nm ([Supplement 1](#), section 5C), which agree well with direct measurements of sidewall roughness on SiN waveguides [61]. These scaling laws allow us to determine the necessary waveguide cross-section at a desired wavelength to achieve an absorption-dominated loss, as illustrated in Fig. 4(c). By increasing the waveguide width to reduce the modal overlap with the sidewalls, we move from a scattering-dominated to an absorption-dominated regime,

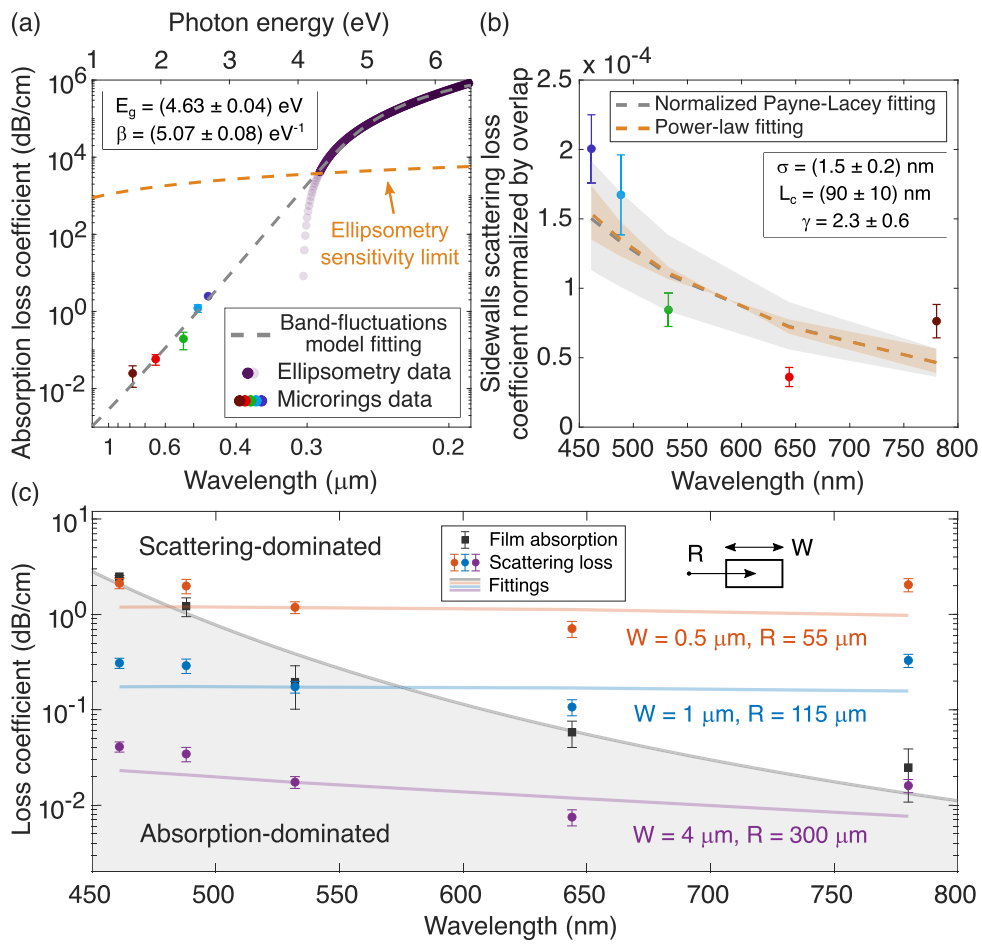


Fig. 4. Wavelength dependence of absorption and surface scattering of the integrated SiN platform ($\text{Si}/\text{N} = 0.82$). (a) Absorption loss coefficient. Ellipsometry (violet dots) only provides reliable readings (opaque violet dots) down to its sensitivity for thin films (orange dashed line, $k \sim 0.002$ [59]), below which it underestimates the film's loss (translucent violet dots) (Supplement 1, section 1A). The band-fluctuations model fitting yields an optical bandgap of $E_g = (4.63 \pm 0.04) \text{ eV}$ and an Urbach slope of $\beta = (5.07 \pm 0.08) \text{ eV}^{-1}$. (b) Sidewall scattering loss coefficient normalized by modal overlap. The NPL model fitting yields a RMS roughness of $\sigma = (1.5 \pm 0.2) \text{ nm}$ and a correlation length of $L_c = (90 \pm 10) \text{ nm}$. The power-law fitting of the type $\lambda^{-\gamma}$ yields $\gamma = (2.3 \pm 0.6)$. The shaded areas depict the fitting uncertainties. We describe the models, datapoints, errorbars, and fittings in Supplement 1, section 5. (c) Wavelength dependence of the surface scattering and absorption loss contributions for varying waveguide widths (W) and radii (R). We obtain the surface scattering loss for each cross-section by multiplying the datapoints and NPL fitting of Fig. 4(b) by their respective sidewalls overlaps (Supplement 1, section 5C).

approaching the fundamental loss limit of the integrated platform. In Figs. 4(a), b, we derive the microring-based datapoints from the fitted α_{abs} and α_{sides} of the reference waveguides at each wavelength, taking into account the confinement and the sidewalls overlap of their optical modes (Supplement 1, section 5). In Fig. 4(c), we obtain the surface scattering loss for different waveguide cross-sections by multiplying the datapoints and NPL fitting in Fig. 4(b) by their respective sidewalls overlaps (Supplement 1, section 5C).

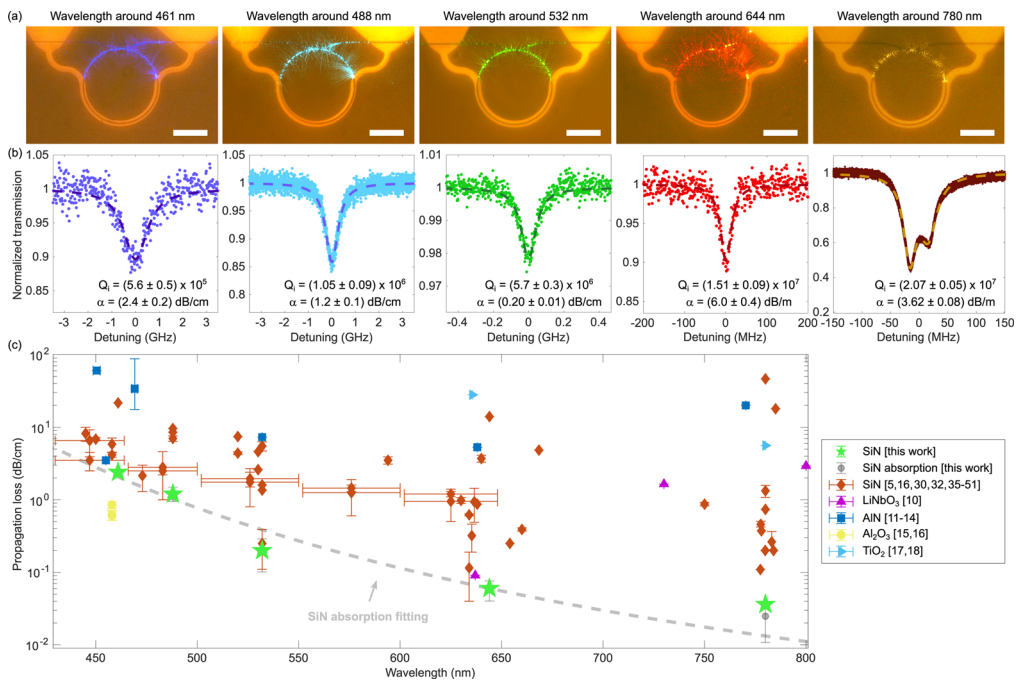


Fig. 5. Ultra-low loss, high-confinement microring resonators from deep visible to near-infrared wavelengths. (a) Examples of microresonators on resonance at the measured wavelengths (461 nm, 488 nm, 532 nm, 644 nm, and 780 nm) (Methods, section 5.2). Scale bar: 50 μm . (b) Highest quality factors, corresponding to the fundamental TE modes of microresonators with 4 μm width. The ring radius is 115 μm for 461 nm, and 300 μm for the other wavelengths. The errorbars correspond to the mean \pm s.d. of tens of consecutive measurements for all the recorded laser detunings of each resonance (e.g., Fig. 3(b)). (c) Propagation losses of state-of-the-art high-confinement integrated platforms. Our losses are the lowest among high-confinement SiN platforms to date and approach the absorption limit of our film (gray datapoints and dashed line fitting from Fig. 4(a)).

By engineering the modal profile, we demonstrate absorption-dominated propagation losses down to 3.62 dB/m at near-IR (780 nm), 6.0 dB/m at red (644 nm), 0.20 dB/cm at green (532 nm), 1.2 dB/cm at blue (488 nm), and 2.4 dB/cm at deep blue (461 nm), corresponding to intrinsic quality factors of 2.07×10^7 , 1.51×10^7 , 5.7×10^6 , 1.05×10^6 and 5.6×10^5 respectively (Fig. 5). These fundamental TE mode losses are close to the absorption limit of the SiN film (Fig. 4(a)), since the wide microring width of 4 μm minimizes the surface scattering loss (Fig. 4(c)). Regardless of the film and microfabrication differences among works in the literature, our results constitute the lowest propagation losses reported in high-confinement SiN platforms to date (Fig. 5(c)). They are also the lowest losses in any high-confinement platform, except for wavelengths approaching 450 nm or shorter where Al₂O₃ yields lower absorption due to its larger optical bandgap. We present the measured losses of the fundamental TE and TM modes for all the other widths and radii in [Supplement 1](#), section 4. Our results demonstrate that the proper design of the waveguide cross-section is effective in approaching the absorption-limited loss of an integrated platform regardless the quality of the waveguide sidewalls.

4. Discussion

Using our ultra-high Q, high-confinement SiN platform, we demonstrate how to probe, model and approach the fundamental loss limits of a photonic integrated platform, which is pivotal for realizing large-scale integrated systems and ultra-narrow-linewidth chip-scale lasers. By leveraging the sensitivity of microring resonators to loss, we use microresonators of different geometries to discriminate and extract the absorption and surface scattering losses of the platform with unparalleled accuracy and sensitivity across the visible spectrum. Our strategy overcomes the limitations of current loss measurement techniques, enabling the determination of the dominating source of loss for arbitrary waveguide cross-sections at a desired wavelength. Through the derived loss scaling laws, our method also provides elusive critical information about the film and microfabrication that quantifies their quality, such as optical bandgap, Urbach slope and sidewall roughness. We show that by engineering the optical mode overlap with the sidewalls, we approach the absorption-limited loss of the platform regardless of the waveguide sidewall roughness, achieving the lowest propagation losses of a high-confinement SiN platform at visible wavelengths to date. While we focused on the visible spectrum, where high losses have hindered the development of dense and scalable chip-scale systems, our strategy is applicable to any material platform and spectral range. Our microheater-based measurement is indifferent to material and geometrical properties, making it particularly suitable for deposited amorphous films that have played a decisive role in the photonics industry. Our measured surface scattering scaling of $\lambda^{-2.3}$ also emphasizes its different nature from volumetric Rayleigh scattering (λ^{-4} scaling [62]), highlighting the importance of using dense films with minimal defects such as from LPCVD (Supplement 1, section 2) to suppress additional scattering at short wavelengths. We envision our techniques for loss characterization and minimization to be key contributors for the development of large-scale PICs that redefine the loss limits of integrated platforms across the electromagnetic spectrum.

5. Methods

5.1. Fabrication methods

To fabricate the SiN photonic chips, we first grew 2 μm of wet thermal SiO₂ on two silicon wafers. Next, we deposited 275 nm of SiN using different LPCVD recipes for each wafer. The recipes use ammonia (NH₃) and dichlorosilane (SiH₂Cl₂, DCS) as reacting gases and deposition temperatures around 800 °C. After the depositions, we polished the films using Celexis CX94S slurry and a Politex Supreme pad [23,63] to smoothen the films' top surfaces. We then patterned the devices using 2-pass electron-beam lithography in a JEOL JBX9500FS system, and the low-loss etch process described in [23,63] using a Oxford Plasmalab 100 system. We cladded the PICs with 1 μm of LPCVD Low Temperature Oxide (LTO). For the microheaters, we used a metal lift-off process based on contact photolithography and metal sputtering to pattern 100 nm of platinum on a titanium adhesion layer. The mask aligner was a SUSS MicroTech MA/BA 6 Contact Aligner, and the sputtering machine was an AJA sputtering tool. Finally, we defined the facets of the PICs by Bosch-etching 150 μm into the silicon substrate using a Unaxis 770 Deep Silicon Etcher, and diced the wafers to separate the chips using a Disco DAD3220 dicing saw.

5.2. Experimental setup

The wavemeter, signal generator, oscilloscope and photodetector used in the microresonator measurements are respectively a HighFinesse WS7-60, a Keysight 33512B Waveform Generator, a Picoscope 5444B, and a Thorlabs APD120A2. The camera used for the microscope images in Fig. 5(a) is a Thorlabs DCC1645C. The camera's built-in infrared filter and sensor color sensitivities cause the dark red light at 780 nm to artificially look yellow. The employed narrow-linewidth lasers and their respective center wavelengths are: Toptica DL Pro 780 nm for

780 nm; Sacher Lion Series TEC-500-0645-010-M for 644 nm; Cobolt Samba 1500 coupled to a Fiber-Q G&H AOM driven at 170 MHz for 532 nm; Toptica DL Pro HP 488 nm for 488 nm; and Toptica DL Pro HP 461 nm for 461 nm.

Funding. Army Research Office (W911NF2110286); U.S. Department of Energy (BNL No. 390033); National Science Foundation (NNCI-2025233).

Acknowledgments. This work was supported in part by the Novel Chip-Based Nonlinear Photonic Sources from the Visible to Mid-Infrared funded by the Army Research Office under award no. W911NF2110286, and in part by the Co-Design Center for Quantum Advantage (C2QA) funded by the U.S. Department of Energy under award BNL No. 390033. The photonic chips fabrication was done in part at the City University of New York Advanced Science Research Center NanoFabrication Facility, in part at the Columbia Nano Initiative (CNI) Shared Lab Facilities at Columbia University, and in part at the Cornell NanoScale Facility, a member of the National Nanotechnology Coordinated Infrastructure (NNCI), which is supported by the National Science Foundation (Grant NNCI-2025233). We thank A. Gaeta and S. Will for lending critical pieces of equipment for the experiments. We also thank J. R. Rodrigues, A. Gil-Molina, and R. Synowicki (from J.A. Woollam Company) for helpful discussions. M.C.-Z. thanks N. Janosik for her support and helpful discussions.

Disclosures. The authors declare no conflicts of interest.

Data availability. Data underlying the results are presented throughout the paper and its Supplemental Information, and additional data may be obtained from the authors upon reasonable request.

Supplemental document. See [Supplement 1](#) for supporting content.

References

1. R. J. Niffenegger, J. Stuart, C. Sorace-Agaskar, *et al.*, “Integrated multi-wavelength control of an ion qubit,” *Nature* **586**(7830), 538–542 (2020).
2. G. Moody, V. J. Sorger, D. J. Blumenthal, *et al.*, “2022 roadmap on integrated quantum photonics,” *JPhys Photonics* **4**(1), 012501 (2022).
3. K. K. Mehta, C. Zhang, M. Malinowski, *et al.*, “Integrated optical multi-ion quantum logic,” *Nature* **586**(7830), 533–537 (2020).
4. A. Mohanty, Q. Li, M. A. Tadayon, *et al.*, “Reconfigurable nanophotonic silicon probes for sub-millisecond deep-brain optical stimulation,” *Nat. Biomed. Eng.* **4**(2), 223–231 (2020).
5. W. D. Sacher, X. Luo, Y. Yang, *et al.*, “Visible-light silicon nitride waveguide devices and implantable neurophotonic probes on thinned 200 mm silicon wafers,” *Opt. Express* **27**(26), 37400–37418 (2019).
6. D. Kohler, G. Schindler, L. Hahn, *et al.*, “Biophotonic sensors with integrated Si_3N_4 -organic hybrid (sinoh) lasers for point-of-care diagnostics,” *Light: Sci. Appl.* **10**(1), 64 (2021).
7. M. C. Shin, A. Mohanty, K. Watson, *et al.*, “Chip-scale blue light phased array,” *Opt. Lett.* **45**(7), 1934–1937 (2020).
8. J. Notaros, M. Raval, M. Notaros, *et al.*, “Integrated-phased-array-based visible-light near-eye holographic projector,” in *Conference on Lasers and Electro-Optics* (Optica Publishing Group, 2019), paper STu3O.4.
9. M. Raval, A. Yaacobi, and M. R. Watts, “Integrated visible light phased array system for autostereoscopic image projection,” *Opt. Lett.* **43**(15), 3678–3681 (2018).
10. B. Desiatov, A. Shams-Ansari, M. Zhang, *et al.*, “Ultra-low-loss integrated visible photonics using thin-film lithium niobate,” *Optica* **6**(3), 380–384 (2019).
11. W. Shin, Y. Sun, M. Soltani, *et al.*, “Demonstration of green and uv wavelength high q aluminum nitride on sapphire microring resonators integrated with microheaters,” *Appl. Phys. Lett.* **118**(21), 211103 (2021).
12. T.-J. Lu, M. Fanto, H. Choi, *et al.*, “Aluminum nitride integrated photonics platform for the ultraviolet to visible spectrum,” *Opt. Express* **26**(9), 11147–11160 (2018).
13. X. Liu, A. W. Bruch, Z. Gong, *et al.*, “Ultra-high-q uv microring resonators based on a single-crystalline aln platform,” *Optica* **5**(10), 1279–1282 (2018).
14. W. H. Pernice, C. Xiong, and H. X. Tang, “High q micro-ring resonators fabricated from polycrystalline aluminum nitride films for near infrared and visible photonics,” *Opt. Express* **20**(11), 12261–12269 (2012).
15. G. N. West, W. Loh, D. Kharas, *et al.*, “Low-loss integrated photonics for the blue and ultraviolet regime,” *APL Photonics* **4**(2), 026101 (2019).
16. C. Sorace-Agaskar, D. Kharas, S. Yegnanarayanan, *et al.*, “Versatile silicon nitride and alumina integrated photonic platforms for the ultraviolet to short-wave infrared,” *IEEE J. Sel. Top. Quantum Electron.* **25**(5), 1–15 (2019).
17. J. T. Choy, J. D. B. Bradley, P. B. Deotare, *et al.*, “Integrated TiO_2 resonators for visible photonics,” *Opt. Lett.* **37**(4), 539–541 (2012).
18. C. C. Evans, C. Liu, and J. Suntivich, “Low-loss titanium dioxide waveguides and resonators using a dielectric lift-off fabrication process,” *Opt. Express* **23**(9), 11160–11169 (2015).
19. N. Chauhan, J. Wang, D. Bose, *et al.*, “Ultra-low loss visible light waveguides for integrated atomic, molecular, and quantum photonics,” *Opt. Express* **30**(5), 6960–6969 (2022).
20. N. Chauhan, A. Isichenko, K. Liu, *et al.*, “Visible light photonic integrated brillouin laser,” *Nat. Commun.* **12**(1), 4685 (2021).

21. T. J. Morin, L. Chang, W. Jin, *et al.*, "Cmos-foundry-based blue and violet photonics," *Optica* **8**(5), 755–756 (2021).
22. C. A. A. Franken, A. van Rees, L. V. Winkler, *et al.*, "Hybrid-integrated diode laser in the visible spectral range," *Opt. Lett.* **46**(19), 4904–4907 (2021).
23. X. Ji, S. Roberts, M. Corato-Zanarella, *et al.*, "Methods to achieve ultra-high quality factor silicon nitride resonators," *APL Photonics* **6**(7), 071101 (2021).
24. D. J. Blumenthal, R. Heideman, D. Geuzebroek, *et al.*, "Silicon nitride in silicon photonics," *Proc. IEEE* **106**(12), 2209–2231 (2018).
25. G. Sinatkas, T. Christopoulos, O. Tsilipakos, *et al.*, "Electro-optic modulation in integrated photonics," *J. Appl. Phys.* **130**(1), 010901 (2021).
26. K. Liu, C. R. Ye, S. Khan, *et al.*, "Review and perspective on ultrafast wavelength-size electro-optic modulators," *Laser Photonics Rev.* **9**(2), 172–194 (2015).
27. Z. Yong, H. Chen, X. Luo, *et al.*, "Power-efficient silicon nitride thermo-optic phase shifters for visible light," *Opt. Express* **30**(5), 7225–7237 (2022).
28. L. Sirlento and G. C. Righini, "An introduction to nonlinear integrated photonics devices: Nonlinear effects and materials," *Micromachines* **14**(3), 604 (2023).
29. F. Gardes, A. Shooa, G. De Paoli, *et al.*, "A review of capabilities and scope for hybrid integration offered by silicon-nitride-based photonic integrated circuits," *Sensors* **22**(11), 4227 (2022).
30. M. Corato-Zanarella, A. Gil-Molina, X. Ji, *et al.*, "Widely tunable and narrow-linewidth chip-scale lasers from near-ultraviolet to near-infrared wavelengths," *Nat. Photonics* **17**(2), 157–164 (2023).
31. Y. Lin, J. C. C. Mak, H. Chen, *et al.*, "Low-loss broadband bi-layer edge couplers for visible light," *Opt. Express* **29**(21), 34565–34576 (2021).
32. Y. Lin, Z. Yong, X. Luo, *et al.*, "Monolithically integrated, broadband, high-efficiency silicon nitride-on-silicon waveguide photodetectors in a visible-light integrated photonics platform," *Nat. Commun.* **13**(1), 6362 (2022).
33. L. Y. Beliaev, E. Shkondin, A. V. Lavrinenko, *et al.*, "Optical, structural and composition properties of silicon nitride films deposited by reactive radio-frequency sputtering, low pressure and plasma-enhanced chemical vapor deposition," *Thin Solid Films* **763**, 139568 (2022).
34. C. J. Krückel, A. Fülop, Z. Ye, *et al.*, "Optical bandgap engineering in nonlinear silicon nitride waveguides," *Opt. Express* **25**(13), 15370–15380 (2017).
35. E. Shim, Y. Chen, S. Masmnidis, *et al.*, "Multisite silicon neural probes with integrated silicon nitride waveguides and gratings for optogenetic applications," *Sci. Rep.* **6**(1), 22693 (2016).
36. M. Sinclair, K. Gallacher, M. Sorel, *et al.*, "1.4 million q factor Si_3N_4 micro-ring resonator at 780 nm wavelength for chip-scale atomic systems," *Opt. Express* **28**(3), 4010–4020 (2020).
37. S. S. Saseendran, T. D. Kongnyuy, B. Figeyns, *et al.*, "A 300mm cmos-compatible pecvd silicon nitride platform for integrated photonics with low loss and low process induced phase variation," in *Optical Fiber Communications Conference and Exhibition* (2019), pp. 1–3.
38. X. Lu, Q. Li, D. A. Westly, *et al.*, "Chip-integrated visible-telecom entangled photon pair source for quantum communication," *Nat. Phys.* **15**(4), 373–381 (2019).
39. E. S. Hosseini, S. Yegnanarayanan, A. H. Atabaki, *et al.*, "High quality planar silicon nitride microdisk resonators for integrated photonics in the visiblewavelength range," *Opt. Express* **17**(17), 14543–14551 (2009).
40. A. Z. Subramanian, P. Neutens, A. Dhakal, *et al.*, "Low-loss singlemode pecvd silicon nitride photonic wire waveguides for 532–900 nm wavelength window fabricated within a cmos pilot line," *IEEE Photonics J.* **5**(6), 2202809 (2013).
41. G. Liang, H. Huang, A. Mohanty, *et al.*, "Robust, efficient, micrometre-scale phase modulators at visible wavelengths," *Nat. Photonics* **15**(12), 908–913 (2021).
42. X. Lu, G. Moille, A. Rao, *et al.*, "On-chip optical parametric oscillation into the visible: generating red, orange, yellow, and green from a near-infrared pump," *Optica* **7**(10), 1417–1425 (2020).
43. R. R. Domenechetti, Y. Zhao, X. Ji, *et al.*, "Parametric sideband generation in cmos-compatible oscillators from visible to telecom wavelengths," *Optica* **8**(3), 316–322 (2021).
44. C. Doolin, P. Doolin, B. C. Lewis, *et al.*, "Refractometric sensing of li salt with visible-light Si_3N_4 microdisk resonators," *Appl. Phys. Lett.* **106**(8), 081104 (2015).
45. S. Romero-García, F. Merget, F. Zhong, *et al.*, "Silicon nitride cmos-compatible platform for integrated photonics applications at visible wavelengths," *Opt. Express* **21**(12), 14036–14046 (2013).
46. L. Stefan, M. Bernard, R. Guider, *et al.*, "Ultra-high-q thin-silicon nitride strip-loaded ring resonators," *Opt. Lett.* **40**(14), 3316–3319 (2015).
47. A. E. Dorche, C. Raman, and A. Adibi, "Very high-q photonic microdisk resonator in an air-clad, thin-film sin at near-visible wavelengths," in *Conference on Lasers and Electro-Optics* (2021), pp. 1–2.
48. A. E. Dorche, B. Wei, C. Raman, *et al.*, "High-quality-factor microring resonator for strong atom–light interactions using miniature atomic beams," *Opt. Lett.* **45**(21), 5958–5961 (2020).
49. Y. Zhao, X. Ji, B. Y. Kim, *et al.*, "Visible nonlinear photonics via high-order-mode dispersion engineering," *Optica* **7**(2), 135–141 (2020).
50. J. A. Smith, H. Francis, G. Navickaite, *et al.*, "Sin foundry platform for high performance visible light integrated photonics," *Opt. Mater. Express* **13**(2), 458–468 (2023).

51. J. H. Song, T. D. Kongnyuy, B. Troia, *et al.*, "Grating devices on a silicon nitride technology platform for visible light applications," *OSA Continuum* **2**(4), 1155–1165 (2019).
52. K. Luke, Y. Okawachi, M. R. E. Lamont, *et al.*, "Broadband mid-infrared frequency comb generation in a Si_3N_4 microresonator," *Opt. Lett.* **40**(21), 4823–4826 (2015).
53. M. Gao, Q.-F. Yang, Q.-X. Ji, *et al.*, "Probing material absorption and optical nonlinearity of integrated photonic materials," *Nat. Commun.* **13**(1), 3323 (2022).
54. C.-W. Tseng, C.-W. Tsai, K.-C. Lin, *et al.*, "Study of coupling loss on strongly-coupled, ultra compact microring resonators," *Opt. Express* **21**(6), 7250–7257 (2013).
55. Y. Zhao, H. Fu, G. T. Wang, *et al.*, "Toward ultimate efficiency: progress and prospects on planar and 3d nanostructured nonpolar and semipolar ingan light-emitting diodes," *Adv. Opt. Photonics* **10**(1), 246–308 (2018).
56. J. A. Guerra, A. Tejada, J. A. Töfflinger, *et al.*, "Band-fluctuations model for the fundamental absorption of crystalline and amorphous semiconductors: a dimensionless joint density of states analysis," *J. Phys. D: Appl. Phys.* **52**(10), 105303 (2019).
57. F. P. Payne and J. P. R. Lacey, "A theoretical analysis of scattering loss from planar optical waveguides," *Opt. Quantum Electron.* **26**(10), 977–986 (1994).
58. J. Lacey and F. Payne, "Radiation loss from planar waveguides with random wall imperfections," *IEE Proc.-J: Optoelectron.* **137**(4), 282–289 (1990).
59. H. G. Tompkins and E. A. Irene, eds., *Handbook of Ellipsometry* (Springer, 2005).
60. J. Resende, D. Fuard, D. Le Cunff, *et al.*, "Hybridization of ellipsometry and energy loss spectra from xps for bandgap and optical constants determination in sion thin films," *Mater. Chem. Phys.* **259**, 124000 (2021).
61. S. Roberts, X. Ji, J. Cardenas, *et al.*, "Measurements and modeling of atomic-scale sidewall roughness and losses in integrated photonic devices," *Adv. Opt. Mater.* **10**(18), 2102073 (2022).
62. D. J. Lockwood, *Rayleigh and Mie Scattering* (Springer, 2016), pp. 1097–1107.
63. X. Ji, F. A. S. Barbosa, S. P. Roberts, *et al.*, "Ultra-low-loss on-chip resonators with sub-milliwatt parametric oscillation threshold," *Optica* **4**(6), 619–624 (2017).